


RESEARCH ARTICLE OPEN ACCESS

Indium-Free Recombination Junctions on Tunnel Oxide Passivating Contacts for Fully Textured Perovskite/Silicon Tandem Solar Cells

Mario Hanser¹  | Sadaf Ghasemi¹ | Armin Richter¹ | Jana-Isabelle Polzin¹ | Anna Damm¹ | Oliver Fischer^{1,2} | Maryamsadat Heydarian¹ | Oussama Er-Raji^{1,2} | Patricia S. C. Schulze¹ | Paul Llontop³ | Zeinab Eftekhari³ | Monica Morales-Masis³ | Rebecca Saive³ | Jan Benick¹ | Juliane Borchert^{1,2} | Martin Bivour¹ | Stefan W. Glunz^{1,2}

¹Fraunhofer-Institut für Solare Energiesysteme ISE, Freiburg, Germany | ²Department of Sustainable Systems Engineering INATECH, University of Freiburg, Freiburg, Germany | ³MESA+ Institute for Nanotechnology, University of Twente, Enschede, Netherlands

Correspondence: Mario Hanser (mario.hanser@ise.fraunhofer.de)

Received: 19 November 2025 | **Revised:** 10 February 2026 | **Accepted:** 10 February 2026

Keywords: perovskite/silicon tandem solar cells | photovoltaic | renewable energy | TOPCon | transparent conductive oxide

ABSTRACT

A transparent conductive oxide (TCO) acting as a recombination layer in perovskite/silicon tandem solar cells for large-scale industrial production relies on low indium consumption and applicability in a scalable process, such as, for example, direct current sputter deposition. Therefore, we investigate aluminum-doped zinc oxide (AZO) and zinc-doped tin oxide (ZTO) in comparison to commonly used indium tin oxide (ITO) as recombination layers between textured ohmic n-TOPCon substrates and hybrid-processed perovskite solar cells. For TCO deposition on TOPCon, sputter-induced damage is observed that can be cured, enabling a high surface passivation quality and efficient carrier transport. Structural, chemical, and optoelectrical properties of AZO, ZTO, and ITO are studied, and their influence on the hole transport layer formation is investigated. In a second step, perovskite single-junction solar cells on ohmic TCO/n-TOPCon substrates are fabricated to investigate the influence of the TCO variation on device performance. Well-working solar cells on ZTO and ITO are built. A similar tandem solar cell performance is demonstrated when comparing ZTO and ITO recombination layers. Thus, ZTO presents a viable In-free recombination layer deposited in an industrially feasible process without efficiency penalty when compared to ITO.

1 | Introduction

Perovskite/silicon tandem solar cells offer a promising possibility to overcome the efficiency limit of conventional silicon single-junction solar cells and are therefore extensively studied by a fast-growing research community. However, a major part of research and development is conducted on silicon heterojunction (SHJ) technology as bottom solar cell (BSC) [1–4], nowadays reaching a record efficiency of 34.85% [5]. At the same time, the solar cell market is dominated by TOPCon solar cells [6] in the form of the iTOPCon [7–9] solar cell concept, featuring an n-TOPCon electron contact and a diffused p-contact. For this reason, TOPCon BSCs have to be given more focus in research. While

perovskite/silicon tandem solar cell efficiencies around 31% on planar iTOPCon [10, 11], on nanotextured iTOPCon [12, 13], and on TOPCon² [14] BSCs show the feasibility of this technology, there is still a knowledge and performance gap when compared to the mainstream tandem technology on SHJ BSCs. The integration of a perovskite top and a silicon bottom cell into monolithic tandem solar cells requires a recombination layer, which enables efficient charge carrier recombination without significant voltage losses. Transparent conductive oxides (TCO), such as indium tin oxide (ITO) and IZO, are well known and extensively studied for the SHJ single-junction development [15–18]. Therefore, they are nowadays used in a major part of perovskite/silicon tandem

This is an open access article under the terms of the [Creative Commons Attribution](https://creativecommons.org/licenses/by/4.0/) License, which permits use, distribution and reproduction in any medium, provided the original work is properly cited.

© 2026 The Author(s). *Solar RRL* published by Wiley-VCH GmbH.

solar cells and enable the highest efficiencies. At the same time, it is already known that this solution is not suitable for mass production, as the availability of indium (In) is strongly limited [19]. Thus, a successful market entry of perovskite/silicon tandem solar cells not only requires the shift from SHJ to the more industrially relevant TOPCon technology. It further relies on the reduction of In in the transparent conductive electrodes and recombination layers. Therefore, In-free recombination layers, deposited with industrially suited tools, that is, with high throughput and on large areas, and their applicability on TOPCon are of great interest.

Two promising options for In-free recombination junctions have been reported in literature, these options are silicon tunnel junctions [20–25] and In-free TCOs, such as SnO₂ [26], AZO [27, 28], and ZTO [29, 30]. So far SnO₂ is mostly incorporated in n-i-p tandem solar cells [31, 32], a cell design limited by the optical properties of the established hole transport layers (HTL) in the ultraviolet wavelength range when deposited on the front side. Also, the SnO₂ deposition is often limited to lab-scale deposition methods, such as spin-coating, wet chemical bath deposition, or RF sputtering from small planar targets. This issue is resolved by adding Zn as a dopant in ZTO, which not only enables a process with industrially relevant rotary targets but also the direct current (DC) sputter deposition due to the enhanced target conductivity. ZTO is reported as a temperature-stable TCO [33] reaching tandem solar cell efficiencies around 16% in 2016. AZO, on the other hand, is the most used In-free TCO reported in literature. Although tuning the optical and electrical properties of AZO to keep up with conventionally used ITO remains a challenge, well-working perovskite single-junction solar cells on AZO [34–36], as well as perovskite-based tandem solar cells with an AZO recombination layer, have been published [37, 38]. However, so far, no perovskite/silicon tandem device with a state-of-the-art efficiency potential exceeding 30% is presented. Therefore, often unscalable, slow, or expensive deposition techniques, such as pulsed laser deposition [34] or spin-coating are used [31].

In the present work, the three TCOs AZO, ITO, and ZTO are compared with the goal to understand their influence on the perovskite top cell formation and performance. Since the substrate morphology is known to influence the perovskite formation [38, 39], the materials are selected to cover a wide crystallization range from amorphous ZTO to AZO with a rather high crystallinity already after the deposition. As the sputter process induces damage to the underlying TOPCon layer, resulting in reduced surface passivation quality, a curing process is required to restore a high level of surface passivation. In a first step, the material properties of the TCOs as deposited

and after the temperature treatment are investigated. Hall measurements reveal the electrical material properties, while X-ray diffraction (XRD) measurement is used to access the crystallinity of the different materials. The surface roughness is assessed with atomic force microscopy (AFM), since the roughness is not only reported to influence the SAM formation [39] but as well the perovskite crystallinity in the hybrid process [40]. Further, the interaction of the TCOs with Me-4PACz deployed as HTL is assessed with contact angle measurements after different process steps of the perovskite cell processing. Kelvin probe force microscopy measurements are performed to measure the work function (WF) of the TCOs, as well as their influence on the HTL formation. To investigate the substrate dependence of perovskite solar cells, single-junction solar cells are built with the hybrid deposition method [1, 41, 42] for the perovskite absorber on ohmic TCO/n-TOPCon substrates. In a final step, tandem solar cells with two different TCOs are demonstrated to investigate their influence on the recombination mechanism in the tandem configuration under current matching conditions, as well as their implications on the optical device performance.

2 | Sputter Deposition of TCOs on TOPCon

The presented study is conducted on ohmic n-TOPCon substrates, as illustrated in Figure 1a. They consist of n-doped 1 Ω cm silicon wafers textured with regular μm-sized random pyramids with n-TOPCon on both sides. n-TOPCon is hydrogenated after the crystallization anneal. On these substrates, the TCOs are deposited on both sides using a DC-sputtering process with rotary ZTO and ITO targets and a planar AZO target in an inline sputter tool. The optimization of the sputter deposition process of the TCOs on TOPCon was conducted in a previous experiment and is not shown here in detail. This process included variations in power and oxygen levels, as well as different curing procedures. Thus, each process is tuned to minimize sputter-induced damage of the n-TOPCon passivation quality while maintaining a low ohmic contact resistivity. However, the curing of sputter-induced damage on TOPCon builds the basis for the presented experiments. To access the sputter damage, spatially averaged implied V_{OC} (iV_{OC}) calculated from lifetime calibrated photoluminescence (PL) measurements at 1 sun illumination is determined before and after the sputtering process for four samples per group, as well as after the curing anneal, and plotted in Figure 1b. Thereby the curing is performed with a 5 min anneal on a hotplate in air at 300°C. This value is chosen based on a temperature variation presented in Figure S1. The samples are metalized

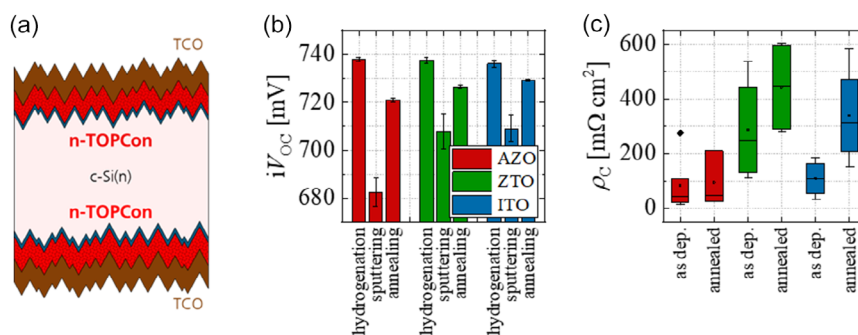


FIGURE 1 | (a) Ohmic n-TOPCon sample structure. (b) iV_{OC} after the process steps of hydrogenation, TCO sputtering and curing anneal for the three TCOs: AZO, ITO and ZTO. (c) TCO/n-TOPCon contact resistivity for all TCOs before and after the curing anneal.

with 1 μm Ag pads after the PL measurements, enabling contact resistivity measurements from the front to the back side.

The initial iV_{OC} after hydrogenation is measured to be close to 740 mV for n-TOPCon substrates. While the iV_{OC} after the sputter deposition of ZTO and ITO reaches around 710 mV, the AZO sputtering process causes the highest damage with iV_{OC} values below 690 mV. The partial pressure of oxygen and the applied sputtering power are often discussed parameters when observing sputter damage. As the AZO deposition is conducted at a lower power than the ZTO deposition and with a lower oxygen partial pressure, it is unlikely that the selected sputter parameters are the origin of the higher surface passivation degradation. More likely are either run-to-run variations or that different target materials cause a different amount of sputter damage. However, a conclusion cannot be drawn at this point. The sputter-induced damage varies from wafer to wafer in a range of 15 mV, represented by the increased scattering observed with four samples. However, a curing anneal could restore a high surface passivation quality for all three materials, this curing is enabled by repassivation of dangling bonds at the silicon interface with surrounding hydrogen [43]. The final iV_{OC} values range between 720 mV and 730 mV. The curing anneal is required to reach the optimal n-TOPCon surface passivation. Since this process can increase the TCO/TOPCon contact resistivity, the contact resistivity is measured as well on four 2.5 by 2.5 cm^2 samples per group and plotted in Figure 1c. AZO shows the lowest contact resistivity in the range of 10 $\text{m}\Omega \text{ cm}^2$ –50 $\text{m}\Omega \text{ cm}^2$ which is not increased during the curing anneal. Measured values for ITO samples are around 100 $\text{m}\Omega \text{ cm}^2$ and for samples with ZTO around 250 $\text{m}\Omega \text{ cm}^2$. These values increase to 300 $\text{m}\Omega \text{ cm}^2$ for ITO-coated samples and 430 $\text{m}\Omega \text{ cm}^2$ for ZTO-coated samples after the curing process. Thus, all samples are well suited as substrates for the subsequent perovskite solar cell investigations, as the contact resistivity only starts to affect the tandem solar cell fill factor (FF) significantly at values around 1 $\Omega \text{ cm}^2$. The correlation between FF and contact resistivity is plotted in Figure S2.

3 | TCO Material Properties and Their Influence on HTL Deposition

In this section, we investigate different material properties of the TCOs, such as their crystallinity, conductivity, WF, and water contact angle. As the surface roughness of a given substrate is known to influence HTL and perovskite formation, the materials

are selected to cover a range of different surface roughness, from amorphous ZTO and ITO, which show a rather planar surface, in contrast to the rougher AZO layer. The difference in surface roughness is confirmed with AFM measurements, which can be found in Figure S3. The TCO material properties are very sensitive to variations in sputter process parameters and therefore easily tunable by adjusting deposition parameters like, for example, power or partial oxygen pressure. The process parameters for the TCO layers investigated in the following are selected based on the investigation of their deposition on TOPCon, the chosen process enables minimal sputter-induced damage while allowing for low ohmic electrical contact. The material properties are assessed in the as-deposited state, as well as after the curing process required for TOPCon. With resolving the influence of the annealing process on the material properties, we aim to gain a deeper understanding of the TOPCon-specific impact on perovskite top solar cells. Therefore, TCO layers are prepared on different substrates for various characterization methods. All layers are deposited with a layer thickness of 30 nm to enable a fair material comparison. The TCOs are sputtered on glass samples to perform Hall effect, XRD, and contact angle measurements. For Kelvin probe measurements the TCOs are deposited on planar and textured silicon wafers. AFM measurements are performed on TCO layers deposited on planar silicon substrates. With contact angle and Kelvin probe force microscopy measurements, the influence of the TCO on the HTL formation is investigated as well. Therefore, Me-4PACz is deposited on the TCO substrates by spin-coating.

In Figure 2a the XRD measurements are plotted before and after the 300°C annealing. The measurements reveal that the annealing process does not induce significant structural changes for ZTO and AZO, as XRD patterns remain unchanged after the annealing. ZTO is mainly amorphous with no visible peaks in the XRD pattern. AZO, on the other hand, already shows a distinct diffraction peak at 34.3° after deposition, corresponding to the (002) [44] crystallographic plane of ZnO and indicating the formation of a polycrystalline film. The XRD pattern of ITO shows no peaks before annealing, an indication of an amorphous material state after sputter deposition. After annealing, a peak at 30.6° appears, which signals solid-phase crystallization of ITO during the annealing process. This peak is associated to the (222) [45] plane of the cubic bixbyite In_2O_3 structure.

An electrical characterization of the TCO layers is performed with Hall effect measurements. The sheet resistance R_{sheet} , the

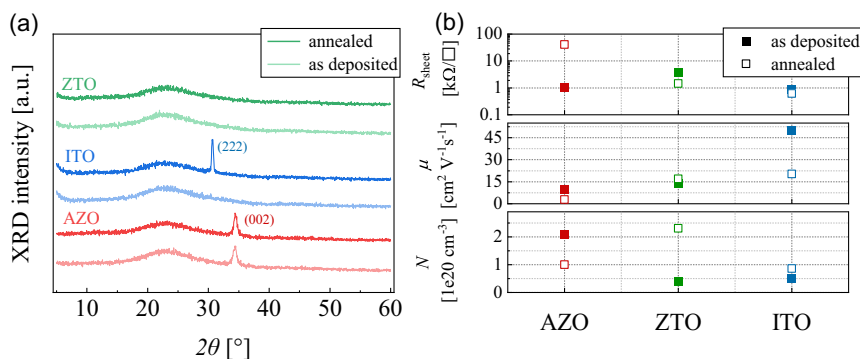


FIGURE 2 | (a) XRD measurements are performed to assess the crystallinity of the TCOs in the as deposited and annealed state, (b) sheet resistance R_{sheet} , the mobility μ and the carrier density N from Hall effect measurements in Van der Pauw configuration.

carrier mobility μ and the carrier concentration N are plotted in Figure 2b. Out of the three compared TCOs, ITO shows the highest lateral conductivity with R_{sheet} below 1 k Ω . This is related to a very high mobility above 45 cm² V⁻¹ s⁻¹ in the as deposited state. After annealing in air, the carrier concentration is increased while the mobility is decreased to around 20 cm² V⁻¹ s⁻¹ at the same time. Thus, the lateral conductivity remains at the same level. ZTO shows a higher sheet resistance up to 4 k Ω having a low carrier concentration of 0.5e20 cm⁻³ and a moderate mobility around 15 cm² V⁻¹ s⁻¹ at the same time. The carrier concentration is increased during the annealing process by a factor of 4, while the mobility is not changed. This results in a decreased lateral resistance. AZO on the other hand shows already after the sputter deposition a very high carrier concentration, which leads to a sheet resistance around 1 k Ω , similar to the one of ZTO after annealing. However, within the annealing process the carrier concentration, and particularly their mobility is drastically reduced for AZO. This results in a high sheet resistance of around 40 k Ω .

In Figure 3a water contact angle and b WF from Kelvin probe force microscopy measurements of the different TCOs are plotted before and after the HTL deposition. For this study, Me-4PACz is deposited by spin-coating after preparing the TCO-coated TOPCon substrates in a 15 min UV-Ozone (UVO) process. After the deposition, the Me-4PACz layer is annealed for 10 min inside a glove box, and the remaining material is subsequently washed away by spin-coating ethanol. Contact angle measurements were additionally performed after the UVO treatment. The contact angle measurements reveal no significant difference in hydrophobicity for the TCO layers before and after annealing. Contact angles around 60° are measured on all considered TCOs. On annealed TCOs, the scattering of the contact angle is reduced when compared to the contact angle on TCOs as deposited. The contact angles drastically drop after the UVO treatment for 15 min. On AZO and ITO, the contact angle drops to values slightly under 20°. On ZTO, the surface becomes even more hydrophilic with the UVO treatment, and contact angles cannot be measured due to the optimal spreading of water on this surface. Contact angle measurements after the HTL deposition are performed to access the SAM uniformity and proper orientation. In this measurement, no difference between the TCOs can be seen. Thus, limitations in surface coverage or molecule orientation can be excluded for the HTL deposition on all TCOs, as this would affect the hydrophobicity and therefore

the water contact angle significantly. With a contact angle average value of 80°, all sample structures show a similar contact angle when compared to SAMs on ITO/SHJ substrates reported in earlier studies [46], which is a promising property for their integration in perovskite solar cells. Measurements of the WF presented in Figure 3b for annealed TCO samples on planar silicon substrates before and after the HTL deposition. Measuring the WF at the surface is generally not representative of the function of a material in the device, as the interface interaction is influenced by both materials forming the interface, for example, through Fermi level pinning or dipole creation. However, specifically for SAM on TCOs, a correlation between the surface WF and the characterized solar cell parameters has been observed in the literature [47], suggesting that this measurement can be useful but must be interpreted with caution. The measurement values present the mean WF of the Kelvin probe force microscopy images provided in Figure S4. The HTL deposition increases the WF of all TCOs significantly, as expected [47, 48]. Despite the WF difference of the TCOs, after HTL deposition, all samples show WFs in a similar order of magnitude, with values between 5.19 eV for ZTO and 5.28 eV for AZO-coated samples. Thus, the WF promises a beneficial band alignment at the HTL/TCO interface for solar cells on all substrates [4, 39].

4 | Perovskite Single Junction Solar Cells

In order to investigate the influence of the different TCOs on the perovskite formation and solar cell performance, single-junction solar cells are processed on different TCO/TOPCon substrates as illustrated in Figure 4.

Therefore, random pyramids of textured n-type wafers are coated symmetrically with n-TOPCon and used as n-type ohmic substrates. These samples feature the same surface properties as a TOPCon² BSC but allow to study the TCO-related influence on the perovskite top cell. The perovskite absorber is processed with the hybrid evaporation/spin-coating method tailored for conformal deposition on industrial standard random pyramids. The solar cell results in terms of JV measurements, iV_{OCs} measured based on PL imaging, and pseudo FF (pFF) values from Suns- V_{OC} imaging are plotted in Figure 5.

Despite reaching the highest iV_{OC} and V_{OC} , the perovskite solar cells on AZO show a very low efficiency, caused by low short circuit current densities and FFs. The origin of this problem

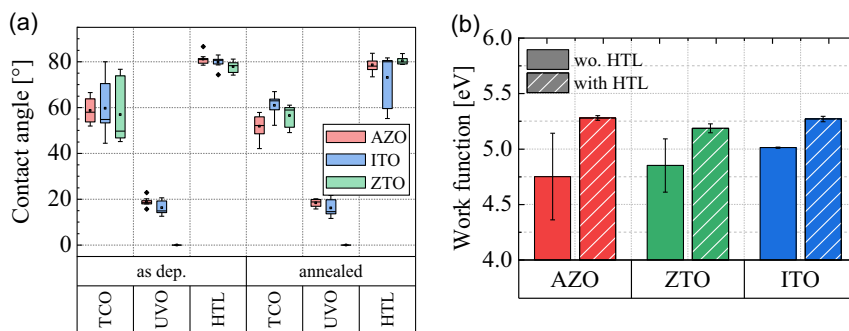


FIGURE 3 | (a) Contact angle measurements on the as deposited and annealed TCO layers, as well as after UV-Ozone (UVO) treatment and HTL deposition. Three samples per group were measured with three measurements on each sample. (b) Work function as mean value of Kelvin probe force microscopy measurements on each sample for annealed TCOs with and without HTL on planar silicon substrates.

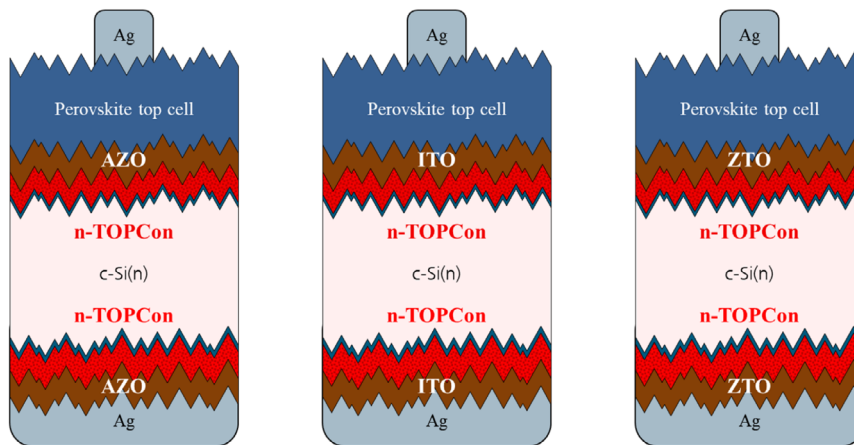


FIGURE 4 | Sketch of the sample structure of perovskite single-junction solar cells on textured ohmic -nTOPCon substrates featuring AZO, ITO, and ZTO recombination layers. For simplicity reasons the same TCO is used for the recombination layer and as rear side contact and is deposited in one process step.

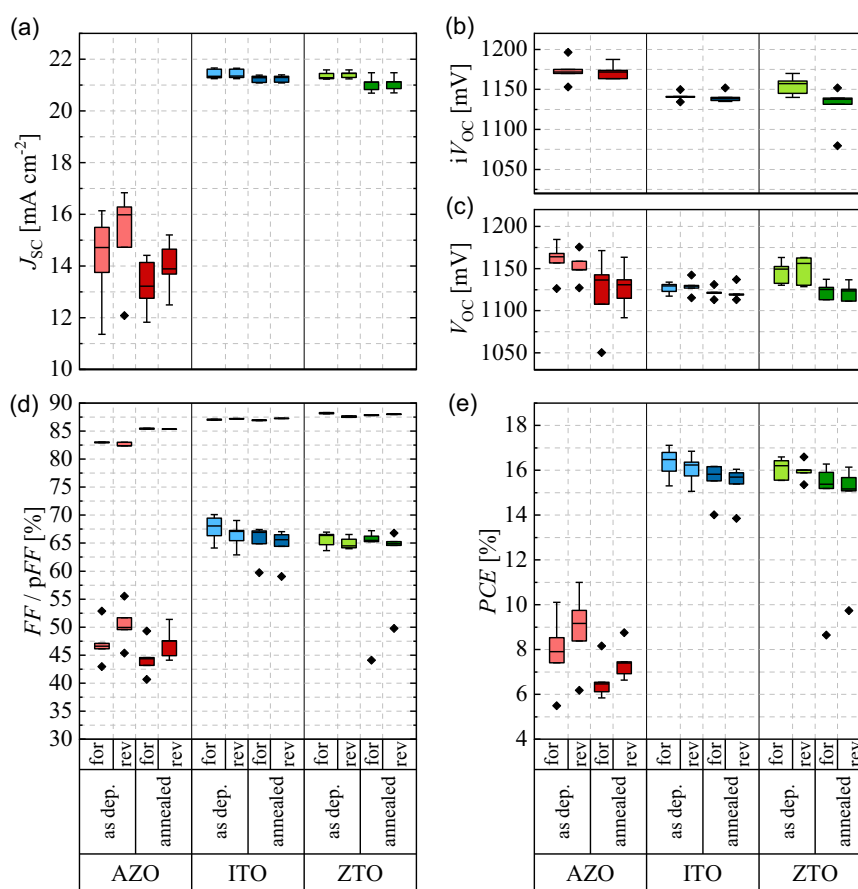


FIGURE 5 | JV parameters of perovskite single-junction solar cells on AZO, ITO, and ZTO consisting of (a) J_{sc} , (b) iV_{OC} , (c) V_{OC} , (d) FF and pFF, and (e) efficiency. Four solar cells per group are measured with forward (for) and reverse (rev) JV -scans.

could not be resolved in this study. Possible explanations could be a low charge carrier mobility along the perovskite/Me-4PACz/AZO contact or the degradation of AZO when in contact with the perovskite solvents. The JV -curves (Figure S5) of these solar cells show a steep decrease in current density around the j_{sc} , which is usually attributed to shunts. However, the pJV -curve (Figure S6), as well as the high pFF, clearly show that these solar cells have high shunt resistivities. This effect can be caused by a low

mobility in one of the solar cells contacts [49]. Perovskite solar cells on ITO and ZTO show very promising JV parameters with efficiencies on a higher level. There is no performance gap between perovskite solar cells on ITO and ZTO. Comparing the V_{OC} of ZTO and ITO, the highest values are observed on ZTO substrates when processed on the ZTO as deposited. This can be explained with the higher iV_{OC} , indicating a higher absorber quality or better passivation. The iV_{OC} and V_{OC} increase

is not observed after the ZTO layer is annealed. Across all ITO and ZTO samples, the V_{OC} follows the same trend as the iV_{OC} , with only a small difference between V_{OC} and iV_{OC} . This indicates minimal selectivity losses in the perovskite solar cell, that is, a well-established hole contact. FFs on ZTO and ITO reach up to 70%, which is slightly below the optimal result of our baseline. The highest values are achieved on ITO substrates, as well showing a small advantage for the material in the as-deposited state. Suns- V_{OC} measurements are performed to further investigate the FF difference when comparing solar cells on ITO and ZTO. The measurements reveal that even though the highest pFFs are measured on ZTO, a lower transport loss on ITO leads to an overall slightly increased FF. This observation is in line with the electrical material characterization presented in Figure 2, which showed a lower conductivity of ZTO due to a lower charge carrier mobility. A comparison of perovskite solar cells on not annealed amorphous and annealed crystalline ITO substrates shows that substrate crystallinity does not significantly affect the properties of the perovskite solar cell. Further, it is observed that even if a high contact angle and WF were regarded as promising properties for the HTL formation, they do not allow a precise forecast of solar cell parameters, as the solar cells on AZO substrates show detrimental limitations even though both measures predict a well-formed HTL.

5 | Perovskite/Silicon Tandem Solar Cells

Based on the results presented in the previous sections, ZTO is identified as a promising option for use as a recombination layer in perovskite/silicon tandem solar cells. Therefore, the performance of tandem solar cells with ZTO and ITO recombination layers on TOPCon² bottom cells is compared in this section. The TOPCon² tandem solar cell design is illustrated in Figure 6 on the left side. The TOPCon² BSCs feature a 110 nm n-TOPCon front contact and a planar 50 nm p-TOPCon rear

contact deposited on a 250 μm thick, 1 $\Omega\text{ cm}$ p-type FZ wafer. The TCO layers on the TOPCon² solar cells are deposited at a thickness of 150 nm on the planar rear side and 30 nm on the textured front side. Thereby one group of solar cells is processed with ITO on the front and rear side, and a second group is processed with ZTO as front and rear contact. All solar cells are finished with a 1 μm Ag layer at the rear side, and the perovskite top cell is processed following the description in the methods section, incorporating the PDAI passivation of perovskite.

On the right side in Figure 6, JV parameters of the TOPCon² tandem solar cells with ITO and ZTO are plotted. These results demonstrate a similar performance of the ITO and ZTO recombination layers in the tandem solar cell configuration. Further, the JV -curves of the devices with the highest PCE and stabilized efficiency measurements can be found in Figures S7 and S8, respectively. JV -curves of both groups are comparable and share similar J_{SCs} and V_{OCs} , as well as FFs. This not only underlines the comparable electrical performance, which was already expected based on the previously presented results [50], but demonstrates as well a similar optical performance. In comparison to the previous results, a slightly lower performance is observed in this batch, which originates in the simplified device structure and a lower surface passivation quality in the SiO_2 passivated dark perimeter region affecting the FF of the tandem device.

External quantum efficiency (EQE) and reflectance measurements are performed for detailed optical analysis of the presented solar cells. Both measurement results are shown in Figure 7 for one exemplary device from each group.

The solar cells used for EQE measurements feature J_{SCs} of 19.6 mA cm^{-2} for the TOPCon² solar cell with ITO recombination layer and 19.7 mA cm^{-2} in case of the TOPCon² solar cell with ZTO recombination layer. These current values, in line with the comparable EQE shapes, as well as the similar reflectance of both solar cells up to 1000 nm, underline the comparable optical performance of ITO and ZTO. However, a difference in reflectance is

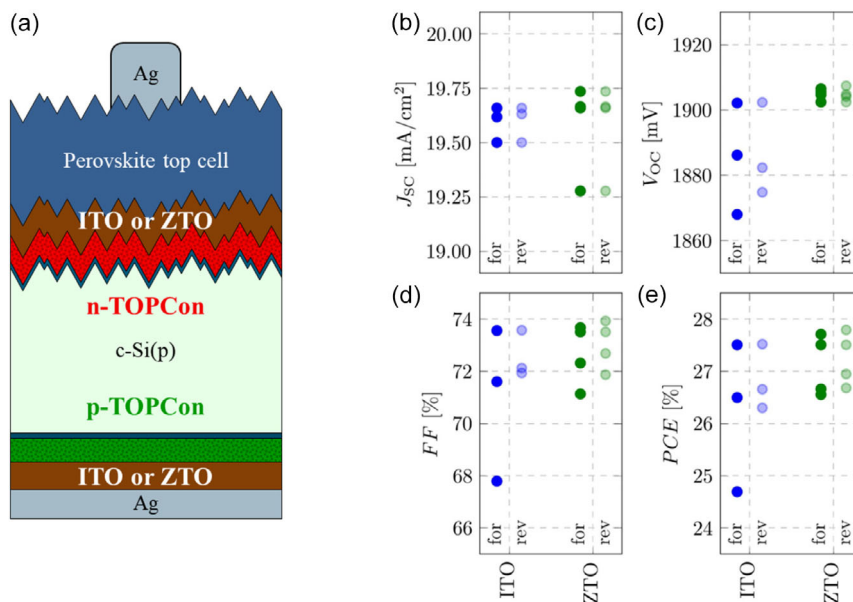


FIGURE 6 | (a) Sketch of the solar cell structure featuring a TOPCon² bottom solar cell with either ITO or ZTO as front and rear side TCO and a fully textured perovskite top solar cell. As well as the JV parameters (b) J_{SC} , (c) V_{OC} , (d) FF, and (e) PCE are plotted for 3–4 devices from each group measured in forward (for) reverse (rev) direction.

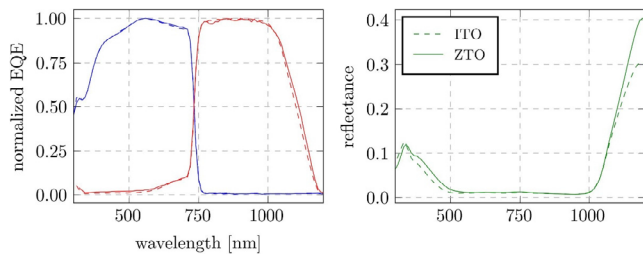


FIGURE 7 | EQE and reflectance measurement of perovskite/silicon tandem solar cells with TOPCon² bottom solar cells and ITO or ZTO recombination layers.

observed at wavelengths above 1100 nm. This behavior does not affect the optical performance of the tandem solar cell but indicates slightly different optical properties. A higher reflectance at 1200 nm is an indication of less parasitic absorption or a better light trapping of the solar cell with ZTO. To disentangle these complex effects, optical simulations would be required, which are not performed here.

6 | Conclusion

In this work, we investigate the influence of different TCOs sputtered on textured n-TOPCon on the performance of fully textured perovskite/silicon tandem solar cells. Therefore, the material properties are analyzed, and their influence on the perovskite solar cell is investigated. As indium is a scarce material but required in the most used TCOs (ITO and IZO), we focus our investigation on the In-free alternatives AZO and ZTO. In a device-level investigation of perovskite single-junction solar cells on ohmic TOPCon substrates with sputtered AZO, ITO, and ZTO, promising results on ITO and ZTO are demonstrated while solar cells on AZO show a detrimental effect on performance independent of annealing prior to perovskite cell processing with low j_{SC} and FFs. As the sputtering of all TCOs induced damage to the underlying TOPCon surface passivation, a curing anneal is required at 300°C. This curing anneal almost fully restores the original surface passivation quality. This annealing of the TCO is observed to only have a minor influence on the perovskite solar cell performance. In perovskite solar cells the integration of ZTO as deposited is, for example, observed to increase the V_{OC} by 20 mV. This increase is not observed after the material was annealed. A detailed material analysis shows a higher crystallinity and surface roughness of AZO, which is in line with the literature. ZTO, on the other hand, is an amorphous material and remains in an amorphous state even after the annealing. ITO is deposited as amorphous material as well and partially crystallized during the annealing process. There was no influence of the ITO crystallinity on the solar cell performance observed. Hall measurements reveal a lower conductivity as well as a lower charge carrier mobility of ZTO when compared to ITO. This effect could be the reason for the slightly varying FFs in perovskite single-junction solar cells. The contact angle, as well as WF measurements, indicates similar HTL properties on all TCOs and is in line with literature reports, this, however, must not necessarily be a good indicator for well-working solar cells.

Finally, the ZTO recombination layer was successfully integrated into TOPCon-based perovskite/silicon tandem solar cells, which demonstrates the feasibility of this material as similar efficiencies

are reached with ITO and ZTO. Thus, ZTO presents a viable In-free recombination TCO on TOPCon BSCs. The DC sputtering from rotary targets thereby enables a process transfer to industrial standard tools with high throughput. This is achieved without performance penalty when compared to ITO and paves the way for In-free recombination TCOs for integration into fully textured perovskite/silicon tandem solar cells based on TOPCon bottom cells.

7 | Experimental Methods

7.1 | Preparation of n-TOPCon Ohmic Substrates

The n-type ohmic TOPCon substrates consist of 1 Ω cm phosphorus-doped 4-inch wafers with <100> orientation, a thickness of 200 μm , and textured surfaces prepared in an alkaline etching process. A thin thermally grown silicon oxide is used as an interfacial oxide and covered by an a-Si layer for TOPCon. The amorphous silicon layers are deposited in situ doped with PECVD (*c.PLASMA, centrotherm*) at a process temperature of 450°C, PH_3 is used as a doping gas, and the target layer thickness is 110 nm. n-TOPCon is then formed in a tube furnace anneal with a 10 min plateau time at 900°C. Hydrogenation is performed with by a PECVD deposition of 100 nm SiN_x at 450°C and a subsequent etch-back of the dielectric layer. Directly before TCO deposition, the natively grown silicon oxide is removed in a 1 min etching process with diluted HF. TCOs are sputtered on the front side only in the active area using a shadow mask with 11 mm by 11 mm windows with a thickness of 30 nm (measured on a planar surface). At the rear side, the TCOs are deposited using the same process as on the front side while a layer thickness of 200 nm is targeted. All TCOs are deposited in an inline tool from Singulus in a DC sputtering process with the capability of a homogeneous deposition over an area of 30 cm by 1 m. ITO (90/10 wt.%, $\text{In}_2\text{O}_3/\text{SnO}_2$) and ZTO (92/8 wt.% SnO_2/ZnO) are sputtered from rotary targets, and AZO (99/1 wt.% $\text{ZnO}/\text{Al}_2\text{O}_3$) is sputtered using a planar target. Thereby, all targets feature the same length of 0.65 m, making the absolute applied power values comparable. All processes are performed at room temperature, and a wafer temperature lower than 60°C can be confirmed during the deposition. Before each deposition, the cathode is operated at the target power for 5 min. ITO deposition is performed with a sputtering power of 700 W and an oxygen gas flow of 20 sccm during the deposition, which results in a dynamic deposition rate of 10 nm m min^{-1} and a process time of 36 s for a 30 nm ITO deposition. For ZTO, 1500 W and 18 sccm oxygen are used resulting in a 22.5 nm m min^{-1} deposition rate and a process time of 16 s. For AZO 1000 W and 2 sccm oxygen gas flow is used. This process has a dynamic deposition rate of 9.65 nm m min^{-1} which leads to a process duration of 38 s for a 30 nm AZO layer deposition. Argon is added for the deposition of all TCOs to reach a fixed total gas flow of 600 sccm, resulting in a pressure of approximately 0.45 Pa. Afterward, the substrates are finished by applying a 300°C curing anneal on the hotplate, evaporating 1 μm of silver on the rear side, and laser cutting the cells into 2.5 cm by 2.5 cm pieces.

7.2 | Preparation of TOPCon² Bottom Solar Cells

TOPCon² BSCs are build using 1 Ω cm boron doped 4-inch wafers with <100> orientation, a thickness of 250 μm and a textured

front surface prepared in an alkaline etching process. The rear side of the solar cell is masked with 100 nm SiN_x during the texturing process and subsequently removed in a buffered oxide etch to maintain the planar surface morphology. A 100 nm SiO_2 layer is thermally grown and removed the front side, as well as on the rear side in the active solar cell area. This layer ensures a separation of the bulk material and the rear emitter in the dark perimeter region, minimizing charge carrier out-diffusion losses. A thin silicon oxide is thermally grown afterwards and covered by an a-Si layer for TOPCon. The amorphous silicon layers are deposited in situ doped with PECVD (*c.PLASMA, centrotherm*) at a process temperature of 450°C, PH_3 is used as doping gas, and the target layer thickness is 110 nm for the front side n-doped layer. In case of p-type layers the targeted layer, thickness is 50 nm and BF_3 is used as doping gas. TOPCon is then formed by crystallization of the amorphous silicon layers in a tube furnace coanneal with 10 min plateau time at 900°C. Hydrogenation is performed with by a PECVD deposition of 100 nm SiN_x at 450°C and a subsequent etch-back of the dielectric layer. Directly before TCO deposition the natively grown silicon oxide is removed in a 1 min etching process with diluted HF. ITO (97/3 wt.%, $\text{In}_2\text{O}_3/\text{SnO}_2$) is sputtered in the Scala tool from vonArdenne and ZTO (92/8 wt.% SnO_2/ZnO) is sputtered using the VISTARIS from Singulus. Afterward, the substrates are finished by applying a 300°C curing anneal on the hotplate, evaporating 1 μm of silver on the rear side, and laser cutting the solar cells into 2.5 cm by 2.5 cm substrates.

7.3 | Preparation of Perovskite Solar Cells

The ohmic TCO/n-TOPCon substrates are prepared for the perovskite processing in a 15 min UVO process and transferred to a glovebox for processing under N_2 atmosphere. Solutions are prepared by mixing 1 mg ml^{-1} Me-4PACz with pure ethanol for the HTL deposition and 83.73 mg ml^{-1} FABr, as well as 115.22 mg ml^{-1} FAI with ethanol for the perovskite absorber. After dissolving the organic components of the perovskite absorber FABr and FAI are mixed with a volume ratio of 72/28 vol% adding 3 mg ml^{-1} of urea [42] for solar cells with PDAI [1] passivation. Processing without PDAI (data presented in Figure 5) passivation is done with a volume ratio of 65/35 vol% of FABr and FAI. The HTL is deposited dropping 100 μl of the prepared solution and starting the spin-coating process with maximum RPM of 5000 after a 7 s waiting time. After the HTL spin-coating, samples are annealed at 100°C for 10 min on a hotplate inside the glovebox and washed subsequently by spin-coating 200 μl ethanol using the same process of dropping the solution dynamically. The inorganic components, 500 nm PbI_2 (beads from Alfa Aesar) and 50 nm CsI (powder from Sigma-Aldrich), of the perovskite are thermally coevaporated and form a conformal scaffold layer over the texture of the BSC. The evaporation rates are set to 0.1 \AA s^{-1} for CsI and 1 \AA s^{-1} for PbI_2 , which are reached at a temperature of 400°C and 280°C, respectively. The substrate temperature is kept at 20°C during this process. The scaffold is then infiltrated by the organic components via spin-coating in the subsequent step. Here, 150 μl of the prepared solution are dynamically dropped on a sample rotating at 2200 RPM for 35 s followed by a 100°C annealing treatment for 10 min in air. For the PDAI passivation, 0.4 mg ml^{-1} PDAI is dissolved in a mixture of chlorobenzene and

isopropanol (50/50 vol%) and dynamically spin-coated on the perovskite absorber and again annealed at 100°C for 3 min in the glovebox. Subsequently, 18 nm of C_{60} are thermally evaporated with a rate of 0.15 \AA s^{-1} at a process temperature of 470°C to form the electron transport layer (ETL). Afterward, 30 nm SnO_x is deposited by atomic layer deposition at a process temperature of 80°C using the deionized water and TDMASn as precursors. As front contact, a 35 nm ITO layer is DC sputtered through a shadow mask in the active area, followed by a thermal evaporation of 300 nm silver at a rate of 2 \AA s^{-1} using a shadow mask to form the busbars and grid fingers. The processing is finished by a thermal evaporation of 140 nm MgF_x incorporated as an antireflection coating.

7.4 | Characterization Methods

XRD measurements of the TCO layers are performed in a Bruker D2 Phaser diffractometer in the range from 5° to 60° for 2θ and a step size of 0.03° and a counting time of 0.15 s per step on TCOs layers with a thickness of 30 nm sputtered on planar $2.5 \times 2.5 \text{ cm}^2$ glass substrates.

Hall effect measurements were performed using a Bruker Magnet B-E 10 electromagnet, operated with a maximum current of 30 A per coil. A Keithley 6220 DC current source and a Keithley 6221 AC/DC current source were employed to provide the excitation current. The Hall voltage was measured in a four-point van der Pauw configuration.

Contact angle measurements are performed with an OCA system from dataphysics. Therefore, 5 μl water drops are placed on the same glass substrates with TCO or HTL/TCO layers with a pipet and captured with a build-in camera.

AFM measurements are performed with a Bruker AFM on 30 nm TCO layers coated on shiny etched FZ crystalline silicon wafers with and without spin-coated Me-4PACz on top. The measurements are performed in peak-force tapping mode, scanning an area of 1 μm by 1 μm .

Kelvin probe force microscopy is performed on 1 μm by 1 μm areas on TCO-coated crystalline silicon wafers with an NX10 scanning probe microscope from Park Systems. The calibration is performed by measuring the WF of highly orientated pyrolytic graphite with a known WF of 4.6 eV before and after the measurement of each TCO. The reported error bars represent the difference of these two values in relation to the measured WF value of the corresponding TCO.

EQE was measured using an in-house setup that included a Xenon lamp as the light source, a double monochromator to produce single-wavelength light, and a lock-in amplifier to detect and enhance the signal-to-noise ratio. The EQE of the perovskite solar cells was measured in the wavelength range of 300–900 nm (with 10 nm steps).

The *JV*-curves of the solar cells were evaluated under standard testing conditions (AM1.5G, 100 mW cm^{-2} , 25°C) using an LED-based solar simulator calibrated based on the spectral response measurements from the EQE setup. The measurement range is set to range from –200 mV to 1300 mV, covered within a measurement time of 40 s.

Suns V_{OC} measurements are performed in a commercial setup from Integro GmbH developed by Fraunhofer ISE consisting of

two lasers, one with a wavelength of 450 nm for the excitation of the perovskite top cell and a second one with a wavelength of 808 nm for the bottom cell excitation. The second laser is not used for this investigation. A power supply is used for V_{OC} and $Suns-V_{OC}$ measurements. $Suns-V_{OC}$ analysis is performed following the procedures published by Fischer et al. [51].

Acknowledgments

The authors would like to thank A. Leimenstoll, F. Schätzle, S. Seitz, T. Wigand, C. Harmel, and R. Neubauer at Fraunhofer ISE for support during the preparation of the samples and characterization. The authors acknowledge the company GfE for co-developing and providing the ZTO target. This work was funded by the German Ministry of Economic Affairs and Climate Action under Grant 03EE1230B (VaPeroTop) and 03EE1192 (EPoBoC) as well as by the Vector Stiftung via their funding of J.B.s research group at Uni Freiburg. M.M.-M. and P.L. acknowledge the financial support by the Dutch Research Council (NWO) as part of the CETPartnership EPoBoC project (EP.1602.22.002).

Open Access funding enabled and organized by Projekt DEAL.

Data Availability Statement

The data that support the findings of this study are available from the corresponding author upon reasonable request.

References

1. O. Er-raji, C. Messmer, R. R. Pradhan, et al., “Electron Accumulation across the Perovskite Layer Enhances Tandem Solar Cells with Textured Silicon,” *Science* 390 no. 6772, (2025): eadx1745, <https://doi.org/10.1126/science.adx1745>.
2. S. Mariotti, E. Köhnen, F. Scheler, et al., “Interface Engineering for High-Performance, Triple-Halide Perovskite-Silicon Tandem Solar Cells,” *Science* 381 (2023): 63–69, <https://doi.org/10.1126/science.adf5872>.
3. X. Y. Chin, D. Turckay, J. A. Steele, et al., “Interface Passivation for 31.25%-Efficient Perovskite/Silicon Tandem Solar Cells,” *Science* 381 (2023): 59–63, <https://doi.org/10.1126/science.adg0091>.
4. E. Aydin, E. Ugur, B. K. Yildirim, et al., “Enhanced Optoelectronic Coupling for Perovskite/Silicon Tandem Solar Cells,” *Nature* 623 (2023): 732–738, <https://doi.org/10.1038/s41586-023-06667-4>.
5. M. A. Green, E. D. Dunlop, M. Yoshita, et al., “Solar Cell Efficiency Tables (Version 66),” *Prog Photovoltaics* 33 (2025): 795–810, <https://doi.org/10.1002/ppv.3919>.
6. ITRPV, “International Technology Roadmap for Photovoltaics (ITRPV),” *Results*. (2024): 2025, <https://www.vdma.org/international-technology-roadmap-photovoltaic>.
7. B. Kafle, B. S. Goraya, S. Mack, F. Feldmann, S. Nold, and J. Rentsch, “TOPCon – Technology Options for Cost Efficient Industrial Manufacturing,” *Solar Energy Materials & Solar Cells* 227 (2021): 111100, <https://doi.org/10.1016/j.solmat.2021.111100>.
8. Y. Chen, D. Chen, C. Liu, et al., “Mass Production of Industrial Tunnel Oxide Passivated Contacts (i-TOPCon) Silicon Solar Cells with Average Efficiency over 23% and Modules over 345 W,” *Progress in Photovoltaics: Research and Applications* 27 (2019): 46, <https://doi.org/10.1002/ppv.3180>.
9. D. Chen, Y. Chen, Z. Wang, et al., “24.58% Total Area Efficiency of Screen-Printed, Large Area Industrial Silicon Solar Cells with the Tunnel Oxide Passivated Contacts (i-TOPCon) Design,” *Solar Energy Materials & Solar Cells* 206 (2020): 110258, <https://doi.org/10.1016/j.solmat.2019.110258>.

10. X. Liao, Y. Zhang, Z. Qu, et al., “Promotion of Grain Growth via Solvent Fumigation for Wide-Bandgap Perovskite Solar Cells with Low VOC Deficit and Perovskite/TOPCon Tandem Solar Cells with Efficiency,” *Science Bulletin* 70 (2025): 2997–3004, <https://doi.org/10.1016/j.scib.2025.05.039>.
11. Y. Luo, Y. Tian, K. Zhao, et al., “Inductive Effects in Molecular Contacts Enable Wide-Bandgap Perovskite Cells for Efficient Perovskite/TOPCon Tandems,” *Nature Communications* 16 (2025): 4516, <https://doi.org/10.1038/s41467-025-59896-8>.
12. L. Wang, N. Wang, X. Wu, et al., “Highly Efficient Monolithic Perovskite/TOPCon Silicon Tandem Solar Cells Enabled by “Halide Locking,”” *Advanced Materials* 37 (2025): 2025–e2416150, <https://doi.org/10.1002/adma.202416150>.
13. R. Li, J. Wang, H. Du, et al., “Optimizing Performance and Stability in Textured 2T Perovskite/Silicon Tandem Photovoltaic Devices through Self-Assembled Monolayer-Mediated Doping Strategies,” *Chemical Engineering Journal* 518 (2025): 164850, <https://doi.org/10.1016/j.cej.2025.164850>.
14. X. Liu, M. Rienäcker, M. Gholipour, et al., “Charge Carrier Management for Highly Efficient Perovskite/Si Tandem Solar Cells with Poly-Si Based Passivating Contacts,” *Energy & Environmental Science* 18 (2025): 5599–5609, <https://doi.org/10.1039/d5ee01486g>.
15. S. de Wolf, A. Descoedres, Z. C. Holman, and C. Ballif, “High-Efficiency Silicon Heterojunction Solar Cells: A Review,” *Green* 2 (2012): 7–24, <https://doi.org/10.1515/green-2011-0018>.
16. Y. Liu, Y. Li, Y. Wu, et al., “High-Efficiency Silicon Heterojunction Solar Cells: Materials, Devices and Applications,” *Materials Science and Engineering: R: Reports* 142 (2020): 100579, <https://doi.org/10.1016/j.mser.2020.100579>.
17. Z. Sun, X. Chen, Y. He, et al., “Toward Efficiency Limits of Crystalline Silicon Solar Cells: Recent Progress in High-Efficiency Silicon Heterojunction Solar Cells,” *Advanced Energy Materials* 12 (2022): 2200015, <https://doi.org/10.1002/aenm.202200015>.
18. H. Lin, M. Yang, X. Ru, et al., “Silicon Heterojunction Solar Cells with up to 26.81% Efficiency Achieved by Electrically Optimized Nanocrystalline-Silicon Hole Contact Layers,” *Nature Energy* 8 (2023), <https://doi.org/10.1038/s41560-023-01255-2>.
19. L. Wagner, J. Suo, B. Yang, et al., “The Resource Demands of Multi-Terawatt-Scale Perovskite Tandem Photovoltaics,” *Joule* 8 (2024): 1142–1160, <https://doi.org/10.1016/j.joule.2024.01.024>.
20. J. Zheng, Z. Ying, Z. Yang, et al., “Polycrystalline Silicon Tunneling Recombination Layers for High-Efficiency Perovskite/Tunnel Oxide Passivating Contact Tandem Solar Cells,” *Nature Energy* 8 (2023): 1250–1261, <https://doi.org/10.1038/s41560-023-01382-w>.
21. F.-J. Haug, A. Morisset, P. Wyss, et al., “Passivating Polysilicon Recombination Junctions for Crystalline Silicon Solar Cells,” *Physica Status Solidi RRL* 15 (2021): 2100272, <https://doi.org/10.1002/pssr.202100272>.
22. C. Luderer, C. Reichel, F. Feldmann, M. Bivour, and M. Hermle, “Passivating and Low-Resistive Poly-Si Tunneling Junction Enabling High-Efficiency Monolithic Perovskite/Silicon Tandem Solar Cells,” *Applied Physics Letters* 115 (2019): 182105, <https://doi.org/10.1063/1.5120552>.
23. C. Luderer, M. Penn, C. Reichel, et al., “Controlling Diffusion in Poly-Si Tunneling Junctions for Monolithic Perovskite/Silicon Tandem Solar Cells,” *IEEE Journal of Photovoltaics* 11 (2021): 1395–1402, <https://doi.org/10.1109/JPHOTOV.2021.3101177>.
24. R. Peibst, M. Rienacker, B. Min, et al., *From PERC to Tandem: POLO-and p + /n + Poly-Si Tunneling Junction as Interface Between Bottom and Top Cell* (2019). accessed March 6, 2019, <https://ieeexplore.ieee.org/document/8533392>.
25. M. Hanser, J. Gry, A. Richter, et al., “Influence of Thermal Activation on Polysilicon Tunnel Junctions for Tunnel Oxide Passivating

- Contacts-Based Perovskite/Silicon Tandem Solar Cells,” *Solar Rrl* 9 (2025): 2400876, <https://doi.org/10.1002/solr.202400876>.
26. M. Härtel, A. Harter, D. Erfurt, et al., “Low Resistivity Sputter Deposited SnO_x Thin Films: An Indium-Free Transparent Conductive Oxide?,” *Phys. Status Solidi RRL* 19 (2025): 2400404, <https://doi.org/10.1002/pssr.202400404>.
27. K. H. Kim, K. C. Park, and D. Y. Ma, “Structural, Electrical and Optical Properties of Aluminum Doped Zinc Oxide Films Prepared by Radio Frequency Magnetron Sputtering,” *Journal of Applied Physics* 81 (1997): 7764–7772, <https://doi.org/10.1063/1.365556>.
28. S. R. Dhage and A. C. Badgujar, “Transparent Conducting Al: ZnO Thin Films on Large Area by Efficient Cylindrical Rotating DC Magnetron Sputtering,” *Journal of Alloys and Compounds* 763 (2018): 504–511, <https://doi.org/10.1016/j.jallcom.2018.05.234>.
29. I.-J. Lee, N.-E. Sung, K. H. Chae, and R. Conley, “Characterization of Zinc-tin-oxide Films Deposited by Radio Frequency Magnetron Sputtering at Various Substrate Temperatures,” *Thin Solid Films* 548 (2013): 385–388, <https://doi.org/10.1016/j.tsf.2013.08.067>.
30. J. Seo and H. Yoo, “Zinc-Tin Oxide Film as an Earth-Abundant Material and Its Versatile Applications to Electronic and Energy Materials,” *Membranes* 12 (2022): 2022, <https://doi.org/10.3390/membranes12050485>.
31. J. Seo and H. Yoo, “Zinc-Tin Oxide Film as an Earth-Abundant Material and Its Versatile Applications to Electronic and Energy Materials,” *Membranes* 12, 2022, <https://doi.org/10.3390/membranes12050485>.
32. F. Gayot, E. Bruhat, M. Bouttemy, et al., “Elucidating Interfacial Limitations Induced by Tin Oxide Electron Selective Layer Grown by Atomic Layer Deposition in N–I–P Perovskite-Based Solar Cells,” *Acs Applied Energy Materials* 6 (2023): 11849–11860, <https://doi.org/10.1021/acsaem.3c01713>.
33. J. Werner, A. Walter, E. Rucavado, et al., “Zinc Tin Oxide as High-Temperature Stable Recombination Layer for Mesoscopic Perovskite/Silicon Monolithic Tandem Solar Cells,” *Applied Physics Letters* 109 (2016): 233902, <https://doi.org/10.1063/1.4971361>.
34. J. W. C. Reinders, J. Bolding, C. Roldán-Carmona, et al., “Room Temperature Pulsed Laser Deposition of Aluminum Zinc Oxide (AZO): Enabling Scalable Indium-Free Transparent Conductive Oxides,” *Advanced Functional Materials* 35 (2025): 2418069, <https://doi.org/10.1002/adfm.202418069>.
35. X. Zhao, H. Shen, Y. Zhang, et al., “Aluminum-Doped Zinc Oxide as Highly Stable Electron Collection Layer for Perovskite Solar Cells,” *Acs Applied Materials & Interfaces* 8 (2016): 7826–7833, <https://doi.org/10.1021/acssami.6b00520>.
36. S. Ghosh, A. Mallick, B. Dou, M. F. van Hest, S. M. Garner, and D. Basak, “A Novel Blanket Annealing Process to Achieve Highly Transparent and Conducting Al Doped ZnO Thin Films: Its Mechanism and Application in Perovskite Solar Cells,” *Solar Energy* 174 (2018): 815–825, <https://doi.org/10.1016/j.solener.2018.09.017>.
37. M. Jošt, E. Köhnen, A. Al-Ashouri, et al., “Perovskite/CIGS Tandem Solar Cells: From Certified 24.2% toward 30% and Beyond,” *ACS Energy Letters* 7 (2022): 1298–1307, <https://doi.org/10.1021/acscenergylett.2c00274>.
38. A. Harter, *Novel Wafer Topographies and Inter-Contact Materials to Enable Industry-Compatible Monolithic Perovskite/Silicon Heterojunction Tandem Solar Cells*. Technische Universität Berlin (2025), <https://doi.org/10.14279/depositonce-23329>.
39. S. Kralj, P. Dally, P. Bampoulis, B. Vishal, S. de Wolf, and M. Morales-Masis, “Impact of the TCO Microstructure on the Electronic Properties of Carbazole-Based Self-Assembled Monolayers,” *ACS Materials Lett* 6 (2024): 366–374, <https://doi.org/10.1021/acsmaterialslett.3c01166>.
40. F. Fu, L. Kranz, S. Yoon, et al., “Controlled Growth of PbI₂ Nanoplates for Rapid Preparation of CH₃NH₃PbI₃ in Planar Perovskite Solar Cells,” *Applications and Materials Science* 212 (2015): 2708–2717, <https://doi.org/10.1002/pssa.201532442>.
41. O. Er-raji, C. Messmer, A. J. Bett, et al., “Loss Analysis of Fully-Textured Perovskite Silicon Tandem Solar Cells: Characterization Methods and Simulation toward the Practical Efficiency Potential,” *Solar RRL* 7 (2023): 2300659, <https://doi.org/10.1002/solr.202300659>.
42. O. Er-raji, M. A. Mahmoud, O. Fischer, et al., “Tailoring Perovskite Crystallization and Interfacial Passivation in Efficient, Fully Textured Perovskite Silicon Tandem Solar Cells,” *Joule* 8 (2024): 1–2833, <https://doi.org/10.1016/j.joule.2024.06.018>.
43. L. Tutsch, F. Feldmann, J. Polzin, et al., “Implementing Transparent Conducting Oxides by DC Sputtering on Ultrathin SiO_x/Poly-Si Passivating Contacts,” *Solar Energy Materials and Solar Cells* 200 (2019): 109960, <https://doi.org/10.1016/j.solmat.2019.109960>.
44. T. Minami, “Transparent Conducting Oxide Semiconductors for Transparent Electrodes,” *Semiconductor Science and Technology* 20 (2005): S35–44.
45. J. H. Kim, K. A. Jeon, G. H. Kim, and S. Y. Lee, “Electrical, Structural, and Optical Properties of ITO Thin Films Prepared at Room Temperature by Pulsed Laser Deposition,” *Applied Surface Science* 252 no.13, (2006): 4834–4837, <https://doi.org/10.1016/j.apsusc.2005.07.134>.
46. J. B. Landgraf, Y. Gupta, A. Prasetyo, et al., “Understanding Postdeposition Treatments of Hole-Transporting Self-Assembling Molecules for Perovskite/Silicon Tandem Solar Cells,” *Advanced Functional Materials* 35, no. 49 (2025): e08186, <https://doi.org/10.1002/adfm.202508186>.
47. N. Singh, A. Mohapatra, C.-W. Chu, and Y.-T. Tao, “Modulation of Work Function of ITO by Self-Assembled Monolayer and Its Effect on Device Characteristics of Inverted Perovskite Solar Cells,” *Organic Electronics* 98 (2021): 106297, <https://doi.org/10.1016/j.orgel.2021.106297>.
48. K. Choi, H. Choi, J. Min, et al., “A Short Review on Interface Engineering of Perovskite Solar Cells: A Self-Assembled Monolayer and Its Roles,” *Solar RRL* 4 (2020): 1900251, <https://doi.org/10.1002/solr.201900251>.
49. S. Akel, Y. Wang, G. Yan, U. Rau, and T. Kirchartz, “Charge Carrier Collection Losses in Lead-Halide Perovskite Solar Cells,” *Advanced Energy Materials* 14 (2024): 2401800, <https://doi.org/10.1002/aenm.202401800>.
50. M. Hanser, A. Richter, J.-I. Polzin, et al., “Fully-Textured Perovskite/Silicon Tandem Solar Cells Exceeding 30% Efficiency on Both Side Tunnel Oxide Passivating Contacted Bottom Cells,” *Solar RRL* 9, no. 24, (2025): e202500835, <https://doi.org/10.1002/solr.202500835>.
51. O. Fischer, A. J. Bett, Y. Zhu, et al., “Revealing Charge Carrier Transport and Selectivity Losses in Perovskite Silicon Tandem Solar Cells,” *Matter* 8, no. 12, (2025): 102404, <https://doi.org/10.1016/j.matt.2025.102404>.

Supporting Information

Additional supporting information can be found online in the Supporting Information section. **Supporting Fig. S1:** Curing anneal variation for ZTO and ITO sputtered on n-TOPCon (left) and p-TOPCon (right). The TCO layers are sputtered on both sides of symmetrical n- and p-type ohmic TOPCon substrates. Sputter induced damage is observed as iV_{OC} decrease after the sputter deposition of ZTO and ITO in a comparable amount. The curing is tested on a hotplate in ambient atmosphere at increasing temperature using the same sample for each step. The optimal curing temperature is found to be 350°C on n-TOPCon and 250°C on p-TOPCon and is independent of the TCO material. For asymmetric solar cells with a n-TOPCon front and a p-TOPCon rear side a curing anneal at 300°C is predicted to yield the optimal result. **Supporting Fig. S2:** Influence of an additional series resistance estimated with a single diode model representing the *JV*-characteristics of silicon single junction solar cell with 26% efficiency and a perovskite/silicon tandem solar cell with

31.6% efficiency. Based on this estimation, we identify a series resistance of $1 \Omega \text{ cm}^2$ as acceptable. **Supporting Fig. S3:** AFM measurements of ITO, ZTO and AZO samples in the as deposited state as well as after the annealing and subsequent Me-4PACz deposition. **Supporting Fig. S4:** Spatially resolved work function obtained from KPFM measurements of the TCOs: AZO, ZTO and ITO as deposited before and after the deposition of Me-4PACz. **Supporting Fig. S5:** Reverse scanned *JV*-curves of perovskite single junction solar cells on annealed (bottom row) and as deposited (top row) AZO, ITO and ZTO coated ohmic TOPCon substrates. Five *JV*-curves of similar processed solar cells are shown for each group. **Supporting Fig. S6:** pseudo *JV* and *JV*-curves of perovskite solar cells on as deposited and annealed AZO, ITO and ZTO coated ohmic n-TOPCon substrates. **Supporting Fig. S7:** *JV*-curves of the best performing perovskite/silicon tandem solar cells with TOPCon² bottom solar cells and a) ITO recombination layer and b) ZTO recombination layer. For both devices a forward and reversed scanned *JV*-curve is plotted and no significant hysteresis is observed. **Supporting Fig. S8:** Stabilized efficiency for all tandem solar cells with ZTO recombination layer compared to a reference device. *PCE* is calculated from fixed voltage measurements at the V_{MPP} extracted from the *JV*-curve scan. For better comparability all curves are normalized. One tandem solar cell with ZTO recombination layer shows the exact same behaviour as the reference solar cell. They show a peak in efficiency a few seconds after starting the measurement and stabilize very close to this peak value after 20–30 s. This tandem solar cell with ZTO recombination layer is the one with the highest efficiency (27.7% measured in reverse *JV*-scan) and shows a stabilized efficiency of 27.6% (not shown in this plot). The three remaining tandem solar cells with ZTO show as well a stable *PCE* after 20–30 s without the maximum at the beginning of the measurement. Overall, this is a promising first measurement for the stability of tandem solar cells featuring a ZTO recombination layer. As reference device a conventional silicon heterojunction based tandem solar cell showing typical properties of our baseline solar cells is used, as there are no measurements available on the TOPCon based tandem solar cells featuring ITO.